

Supporting information

Surfactant-Assisted Synthesis of Semiconductor Hybrid Cd/Hg-Selenidostannates with Enhanced Optoelectronic and Piezoelectric Properties

Mohamed Saber Lassoued ^[a], Yue-Qiao Hu* ^[b], Ahmed Faizan^[a], Yan-Zhen Zheng* ^[a]

^[a] School of Chemistry, Interdisciplinary Research Center of Frontier Science and Technology, Frontier Institute of Science and Technology, State Key Laboratory of Electrical Insulation and Power Equipment, Xi'an Key Laboratory of Electronic Devices and Materials Chemistry, Xi'an Jiaotong University, 99 Yanxiang Road, Xi'an, Shaanxi 710054, P. R. China

^[b] School of Chemistry and Chemical Engineering, Yan'an University, Yan'an, Shaanxi 716000, P. R. China

CONTENTS

1. General Remarks.....	SI-2
2. Characterization methods and Simulation details	SI-2
2.1. Characterization methods	SI-2
2.2. Simulation details	SI-6
2.3. Experimental section	SI-7
2.3.1 Synthesis procedure	SI-7
3. Supporting Tables and Figures	SI-9
4. References	SI-21

* Corresponding author.
E-mail address: zheng.yanzhen@xjtu.edu.cn.
* Corresponding author.
E-mail address: hyq_198505@163.com.

1. General Remarks

Single-crystal X-ray diffraction (SC-XRD) data for the $(\text{H}_2\text{BPP})_2\text{CdSn}_3\text{Se}_9$ and $(\text{H}_2\text{DMP})_2\text{Hg}_4\text{Sn}_4\text{Se}_{15}$ derivatives were collected using a Bruker SMART APEX II CCD diffractometer equipped with graphite-monochromated Mo $K\alpha$ radiation ($\lambda = 0.71073 \text{ \AA}$). The measurements were performed employing the θ - ω scan technique at 298 K. Powder X-ray diffraction (PXRD) intensities were recorded at ambient temperature (298 K) on a Rigaku D/max-III A diffractometer using Cu $K\alpha$ radiation ($\lambda = 1.54056 \text{ \AA}$). The crystalline powder samples were prepared by grinding single crystals and analyzed over a 2θ range of 5° – 50° with a step size of 10° per minute. Solid-state UV-Vis diffuse reflectance spectra of the pressed powder samples were obtained using a SHIMADZU UV-3600 UV-Vis-NIR spectrophotometer, with BaSO_4 powder serving as the reflectance reference. All density functional theory (DFT) calculations were performed using CASTEP within Material Studio 2019. Photocurrent measurements and electrical conductivity assessments were conducted with a Keithley 2400 source meter acting as the voltage source, connected in series with a Keithley 6485 picoammeter to accurately detect the small currents.

2. Characterization Methods and Simulation Details

2.1. Characterization Methods

X-ray Crystallographic Study

Single-crystal X-ray diffraction data for the $(\text{H}_2\text{BPP})_2\text{CdSn}_3\text{Se}_9$ and $(\text{H}_2\text{DMP})_2\text{Hg}_4\text{Sn}_4\text{Se}_{15}$ were collected using a Bruker SMART APEX II CCD diffractometer equipped with graphite-monochromated Mo $K\alpha$ radiation ($\lambda = 0.71073 \text{ \AA}$). Data acquisition was performed employing the θ - ω scan technique at 298 K. The crystal structures were solved by direct methods and subsequently refined using the full-matrix least-squares technique within the SHELXTL program package. ^[S1] All non-hydrogen atoms were refined anisotropically to ensure precise structural determination.

Powder X-ray Diffraction (PXRD)

Powder X-ray diffraction intensities were measured at ambient temperature (298 K) using a Rigaku D/max-III A diffractometer with Cu $K\alpha$ radiation ($\lambda = 1.54056 \text{ \AA}$). The crystalline powder samples were prepared by grinding single crystals to achieve a fine and homogeneous

powder. Measurements were conducted over a 2θ range of 5° – 50° with a scanning rate of 10° per minute to ensure comprehensive phase identification and characterization.

Scanning Electron Microscopy (SEM)

The morphology of the samples was examined using a Gemini SEM 500 Scanning Electron Microscope (Zeiss, Germany). Prior to imaging, the samples were meticulously prepared by sputter-coating with a thin layer of gold to enhance electrical conductivity and minimize charging effects. SEM analysis was conducted at an accelerating voltage of 15 kV, providing high-resolution images that reveal the surface structures and morphological features of the materials. The obtained images facilitated the assessment of particle size, shape, and distribution, thereby offering valuable insights into the material's structural characteristics.

Optical Absorption Measurement

Diffuse reflectance UV-Vis-NIR spectra were acquired at various temperatures using a SHIMADZU UV-3600 UV-Vis-NIR spectrophotometer. Measurements were conducted over a wavelength range of 300 nm to 1200 nm to capture the comprehensive optical behavior of the samples. BaSO₄ powder served as the reflectance reference standard, ensuring accurate calibration and baseline correction of the spectrophotometric data.

The absorption spectra were calculated from the obtained reflectance data using the Kubelka-Munk function, defined by the equation:

$$F(R)=(1-R)^2/2R$$

where:

- **R** is the reflectance,
- **K** represents the absorption coefficient, and
- **S** denotes the scattering coefficient.

This function facilitates the quantitative analysis of the material's optical properties by correlating the reflectance measurements to the intrinsic absorption characteristics. By applying the Kubelka-Munk transformation, the absorption spectra provide valuable insights into the electronic transitions and band structure of the chalcogenide materials under study.

Stability Studies

Freshly prepared perovskite films of $(\text{H}_2\text{BPP})_2\text{CdSn}_3\text{Se}_9$ and $(\text{H}_2\text{DMP})_2\text{Hg}_4\text{Sn}_4\text{Se}_{15}$ were deposited onto clear glass plates using a spin-coating, vapor deposition. After deposition, the glass plates with the perovskite films were placed inside sealed jars containing a saturated solution of $\text{Mg}(\text{NO}_3)_2 \cdot 6\text{H}_2\text{O}$. To minimize light exposure and prevent photodegradation, the sealed jars were stored in the dark. Additionally, the relative humidity within the storage environment was maintained at approximately 55% to simulate controlled atmospheric conditions. [S2]

Importantly, the perovskite films were not in direct contact with the $\text{Mg}(\text{NO}_3)_2 \cdot 6\text{H}_2\text{O}$ solution, ensuring that any observed changes in the films' stability were not influenced by direct chemical interaction with the solution. Over a period of 30 days, the stability of the perovskite films was monitored. After the storage period, the films were carefully removed and subjected to Powder X-ray Diffraction (PXRD) analysis to assess any structural changes or degradation.

Electrode Fabrication

To prepare electrodes for photoelectrochemical measurements, 0.4 g of $(\text{H}_2\text{BPP})_2\text{CdSn}_3\text{Se}_9$ and $(\text{H}_2\text{DMP})_2\text{Hg}_4\text{Sn}_4\text{Se}_{15}$ crystals were first ground into fine powders. The powdered crystals were then dispersed in 1 mL of dimethylformamide (DMF) and subjected to sonication in a water bath to ensure uniform distribution of the samples within the solvent.

Indium Tin Oxide (ITO)-Coated Glass Substrates: The substrates used for electrode fabrication were ITO-coated glass plates with dimensions of $1.0 \times 3.0 \text{ cm}^2$ and a conductivity of $10 \Omega \text{ cm}^{-1}$. These substrates were meticulously cleaned to ensure optimal electrode performance. The cleaning procedure involved:

1. **Sonication in n-Butyl Alcohol:** The ITO-coated glass plates were sonicated in n-butyl alcohol for 30 minutes to remove organic contaminants.
2. **Rinsing with Deionized Water:** Following sonication, the substrates were rinsed several times with deionized water.
3. **Additional Sonication:** The rinsed substrates underwent an additional 15 minutes of sonication in deionized water to ensure thorough cleaning.
4. **Repetition of Cleaning Steps:** Steps 1–3 were repeated multiple times to achieve comprehensive removal of impurities.

5. Vacuum Cleaning: After the sonication and rinsing cycles, the ITO substrates were vacuum-cleaned to eliminate any remaining organic residues.

Coating Process: After cleaning, 20 μL of the $(\text{H}_2\text{BPP})_2\text{CdSn}_3\text{Se}_9$ or $(\text{H}_2\text{DMP})_2\text{Hg}_4\text{Sn}_4\text{Se}_{15}$ ethanol solution was deposited onto each ITO-coated glass substrate. To define the active electrode area and prevent unwanted spreading of the solution, the substrates were masked using 3M Scotch® tape with an effective area of approximately $1.0 \times 1.0 \text{ cm}^2$. The coated substrates were then dried on a hot plate at 65°C for 15 minutes to remove the solvent and ensure proper adhesion of the perovskite material to the ITO surface.

Final Electrode Preparation: Once dried, the electrodes were carefully peeled off from the masking tape, resulting in well-defined active areas suitable for subsequent photoelectrochemical testing. This fabrication process ensured the production of uniform and reproducible electrodes with consistent morphological and compositional properties.

Electrical Conductivity

The electrical conductivity of $(\text{H}_2\text{BPP})_2\text{CdSn}_3\text{Se}_9$ and $(\text{H}_2\text{DMP})_2\text{Hg}_4\text{Sn}_4\text{Se}_{15}$ was measured using pressed pellets prepared from 50 mg of the powdered sample. The powder was finely ground and pressed into pellets with a diameter of 10 mm and a thickness of approximately 0.3 mm using a pellet press. To ensure good electrical contact, silver conductive paint (SPI Supplies Co.) was applied to both the upper and lower surfaces of each pellet, securely attaching the electrical wires.

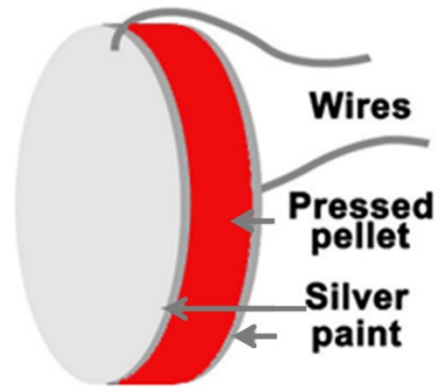
To assess the conductivity under varying temperature conditions, the prepared pellets were placed in an oven where the temperature was precisely controlled. The positive and negative electrodes were connected to the upper and lower surfaces of the pellets, respectively, as illustrated in Scheme 1b. Electrical measurements were conducted using a Keithley 2400 SourceMeter configured as a voltage source, in series with a Keithley 6485 Picoammeter to accurately detect the small currents generated.

The electrical conductivity (σ) was calculated from the current density (\mathbf{J}) versus electric field strength (\mathbf{E}) (J-E) curves based on Ohm's law:

$$\sigma = JE, J = IS, E = VL$$

where:

- σ is the electrical conductivity (S/m),
- J is the current density (A/m²),
- E is the electric field strength (V/m),
- I is the current (A),
- V is the voltage (V),
- S is the cross-sectional area of the pellet (m²),
- L is the thickness of the pellet (m).



Scheme 1. Conductivity test device

The cross-sectional area (S) was determined based on the pellet dimensions, and the thickness (L) was measured using a micrometer. By plotting the current density against the electric field strength, the electrical conductivity was derived from the linear regions of the J-E curves, providing accurate measurements of the material's electrical properties under different thermal conditions.

Piezoelectric Device Fabrication and Characterization

Piezoelectric devices were fabricated using single crystals of $(\text{H}_2\text{BPP})_2\text{CdSn}_3\text{Se}_9$. The single crystals were first meticulously cleaned with acetone and ethanol to eliminate surface contaminants, ensuring pristine surfaces for optimal device performance. Electrical contacts were established by applying silver conductive paint (SPI Supplies Co.) to both the top and bottom faces of each crystal, facilitating reliable electrical connections. To protect the crystals and enhance device stability, the mounted crystals were encapsulated with a thin layer of polyimide. The assembled devices were then subjected to piezoelectric measurements using a PiezoForce Microscopy (PFM) setup, where mechanical stress was applied to the crystals and the resulting electrical responses were accurately recorded. High-resolution PFM imaging confirmed robust piezoelectric behavior, demonstrating significant correlations between applied mechanical stress and generated electrical signals. These results validate the efficacy of $(\text{H}_2\text{BPP})_2\text{CdSn}_3\text{Se}_9$ single crystals for applications in energy harvesting, sensing, and actuation technologies, highlighting their potential in advanced electronic and optoelectronic systems.

2.2. Simulation Details: Computational Methods

The crystallographic data of $(\text{H}_2\text{BPP})_2\text{CdSn}_3\text{Se}_9$ and $(\text{H}_2\text{DMP})_2\text{Hg}_4\text{Sn}_4\text{Se}_{15}$, obtained from single-crystal X-ray diffraction (XRD) analyses, were utilized to compute the electronic band structures and partial densities of states (PDOS). All computational studies were conducted using Density Functional Theory (DFT) as implemented in the BIOVIA Materials Studio Simulation Package. ^[S3, S4]

For the electronic structure calculations, the Generalized Gradient Approximation (GGA) with the Perdew Burke Ernzerhof (PBE) functional was employed. ^[S5, S6] The self-consistent field (SCF) convergence threshold was set to 2×10^{-6} eV/atom to ensure precise convergence of the electronic states. An ultrasoft pseudopotential in the OTFG mode was utilized, and the plane-wave energy cutoff was established at 489.8 eV to balance computational efficiency with accuracy.

The DFT calculations for the band structure of $(\text{H}_2\text{BPP})_2\text{CdSn}_3\text{Se}_9$ and $(\text{H}_2\text{DMP})_2\text{Hg}_4\text{Sn}_4\text{Se}_{15}$ were performed without considering Spin-Orbit Coupling (SOC) to simplify the computational model. These calculations were executed on an elastic compute server equipped with 24 cores and 96 GB of memory, facilitating efficient processing of the complex electronic structures.

These computational parameters were carefully selected to accurately model the electronic properties of $(\text{H}_2\text{BPP})_2\text{CdSn}_3\text{Se}_9$ and $(\text{H}_2\text{DMP})_2\text{Hg}_4\text{Sn}_4\text{Se}_{15}$ while maintaining computational feasibility. The resulting band structures and PDOS provided critical insights into the material's electronic behavior under the specified thermal conditions, complementing the experimental findings.

2.3. Experimental Section

Materials

Tin (Sn) and Selenium (Se), Cadmium Chloride (CdCl_2), Mercury Chloride (HgCl_2), 1, 3-bis(4-piperidiny)propane (BPP), 1, 5-diamino-2-methylpentane (DMP) and PEG-400.

2.3.1 Syntheses of $(\text{H}_2\text{BPP})_2\text{CdSn}_3\text{Se}_9$

Bright red block crystals of $(\text{H}_2\text{BPP})_2\text{CdSn}_3\text{Se}_9$ were synthesized by reacting tin (Sn) and selenium (Se) in a mixed solvent system comprising 1,3-bis(4-piperidiny)propane (BPP) and polyethylene glycol 400 (PEG-400). The reaction mixture was heated to 190 °C and maintained

at this temperature for six days under controlled conditions. This extended heating period facilitated the formation of well-defined red crystalline blocks, indicative of successful synthesis. The reactants were cooled to normal temperature at a rate of 5 °C/h to obtain, sheets and plate like crystals (Yield: ca. 23% based on Cd).

2.3.2 Syntheses of $(\text{H}_2\text{DMP})_2\text{Hg}_4\text{Sn}_4\text{Se}_{15}$

Yellow stick crystals of $(\text{H}_2\text{DMP})_2\text{Hg}_4\text{Sn}_4\text{Se}_{15}$ were synthesized by heating a stoichiometric mixture of tin (Sn), selenium (Se), mercury(II) chloride (HgCl_2), and 1,5-diamino-2-methylpentane (DMP) in polyethylene glycol 400 (PEG-400) as the solvent. The reaction mixture was heated to 160 °C and maintained at this temperature to facilitate crystal growth. Upon completion of the heating process, the yellow stick crystals were obtained, filtered, and subsequently washed with ethanol to remove any unreacted materials and impurities. The purified crystals were then dried under ambient conditions to yield the final product with high purity and crystallinity (Yield: ca. 27% based on Hg).

4. Supporting Tables and Figures

Table S1 Summary of crystal data and structural refinements of **(H₂BPP)₂CdSn₃Se₉** and **(H₂DMP)₂Hg₄Sn₄Se₁₅**

	(H₂BPP)₂CdSn₃Se₉	(H₂DMP)₂Hg₄Sn₄Se₁₅
Empirical formula	C ₂₆ H ₅₆ N ₄ CdSn ₃ Se ₉	C ₁₂ H ₃₆ N ₄ Hg ₄ Sn ₄ Se ₁₅
Formula weight	1603.93	2898.04
Crystal dimensions (mm)	0.12*0.21*0.16	0.11*0.17*0.14
Crystal system	Monoclinic	Orthorhombic
Space group	C c	C m c a
<i>a</i> /Å	17.143(4)	21.470(12)
<i>b</i> /Å	28.047(6)	30.073(17)
<i>c</i> /Å	15.5239(11)	17.988(10)
α /°	90	90
β /°	123.359(3)	90
γ /°	90	90
Volume/Å ³	4564.1(19)	11614(11)
Z	4	8
ρ calcg/cm ³	2.334	3.058
μ /mm ⁻¹	9.282	21.637
F(000)	2960	9040.0
Index ranges	-20<= <i>h</i> <=20, -33<= <i>k</i> <=33, -13<= <i>l</i> <=13	-25<= <i>h</i> <=25, -35<= <i>k</i> <=35, -21<= <i>l</i> <=21
Data Completeness	99.50%	99.60%
Data/restraints/parameters	6257/154/388	5200/68/181
Goodness-of-fit on F ²	1.06	1.06
Weight	$w = 1/[\sigma^2(\text{Fo}^2) + (0.0571\text{P})^2 + 9.4616\text{P}]$ where $\text{P} = (\text{Fo}^2 + 2\text{Fc}^2)/3$	$w = 1/[\sigma^2(\text{Fo}^2) + (0.0789\text{P})^2 + 426.2405\text{P}]$ where $\text{P} = (\text{Fo}^2 + 2\text{Fc}^2)/3$
$R = \sum \text{Fo} - \text{Fc} / \sum \text{Fo} , wR_2$	$R_1 = 0.036, wR_2 = 0.107$	$R_1 = 0.048, wR_2 = 0.156$

$$R_1 = \sum ||\text{Fo} - \text{Fc}|| / \sum |\text{Fo}|, wR_2 = [\sum w(\text{Fo}^2 - \text{Fc}^2)^2 / \sum w(\text{Fo}^2)^2]^{1/2}$$

Table S2 Summary of selected bond lengths (Å) and bond angles (°) of (H₂BPP)₂CdSn₃Se₉

Bond	Lengths/Å	Bond pair	Angles / °
Cd1 Se4	2.6431(16)	Se5 Cd1 Se4	96.10(4)
Cd1 Se5	2.6328(14)	Se5 Cd1 Se7	113.26(4)
Cd1 Se7	2.6398(15)	Se5 Cd1 Se9	112.52(5)
Cd1 Se9	2.6405(15)	Se7 Cd1 Se4	111.01(6)
Sn1 Se1	2.4541(15)	Se7 Cd1 Se9	112.12(5)
Sn1 Se2	2.5672(14)	Se9 Cd1 Se4	110.80(5)
Sn1 Se3	2.5677(14)	Se1 Sn1 Se2	105.69(5)
Sn1 Se4	2.4786(14)	Se1 Sn1 Se3	106.19(5)
Sn2 Se2	2.5675(13)	Se1 Sn1 Se4	112.24(6)
Sn2 Se5	2.4783(13)	Se2 Sn1 Se3	108.86(5)
Sn2 Se6	2.5547(13)	Se4 Sn1 Se2	112.84(5)
Sn2 Se7	2.4948(12)	Se4 Sn1 Se3	110.68(5)
Sn3 Se3	2.5733(15)	Se5 Sn2 Se2	108.31(5)
Sn3 Se6	2.5569(14)	Se5 Sn2 Se6	103.01(4)
Sn3 Se8	2.4588(13)	Se5 Sn2 Se7	110.57(4)
Sn3 Se9	2.4935(14)	Se6 Sn2 Se2	107.91(4)
Se5 Cd1	2.6328(14)	Se7 Sn2 Se2	112.15(4)
		Se7 Sn2 Se6	114.36(4)
		Se6 Sn3 Se3	107.24(5)
		Se8 Sn3 Se3	104.09(5)
		Se8 Sn3 Se6	104.28(5)
		Se8 Sn3 Se9	114.06(5)
		Se9 Sn3 Se3	115.30(5)
		Se9 Sn3 Se6	110.99(5)
		Sn1 Se2 Sn2	106.89(5)
		Sn1 Se3 Sn3	107.03(5)
		Sn1 Se4 Cd1	106.18(5)
		Sn2 Se5 Cd1	105.70(4)
		Sn2 Se6 Sn3	107.96(4)
		Sn2 Se7 Cd1	103.30(4)
		Sn3 Se9 Cd1	103.94(5)

Table S3 Summary of selected bond lengths (Å) and bond angles (°) of (H₂DMP)₂Hg₄Sn₄Se₁₅

Bond	Lengths/Å	Bond pair	Angles / °	Bond pair	Angles / °
Hg1 Se2	2.626(2)	Se2 Hg1 Se2	118.41(10)	Se3 Sn2 Se9	111.45(7)
Hg1 Se2	2.626(2)	Se2 Hg1 Se3	106.02(6)	Se3 Sn2 Se9	111.45(7)
Hg1 Se3	2.739(3)	Se2 Hg1 Se3	106.02(6)	Se3 Sn2 Se1	117.56(10)
Hg1 Se4	2.592(3)	Se4 Hg1 Se2	110.01(5)	Se9 Sn2 Se9	117.38(12)
Hg2 Se4	2.651(3)	Se4 Hg1 Se2	110.01(5)	Se9 Sn2 Se1	99.10(6)
Hg2 Se5	2.627(2)	Se4 Hg1 Se3	105.43(8)	Se9 Sn2 Se1	99.10(6)
Hg2 Se5	2.627(2)	Se5 Hg2 Se4	105.07(6)	Sn1 Se1 Sn1	106.01(11)
Hg2 Se6	2.609(3)	Se5 Hg2 Se4	105.07(6)	Sn1 Se2 Hg1	102.79(8)
Sn3 Se6	2.519(3)	Se5 Hg2 Se5	110.11(12)	Sn2 Se3 Hg1	108.39(10)
Sn3 Se7	2.485(2)	Se6 Hg2 Se4	109.21(8)	Hg1 Se4 Hg2	109.54(9)
Sn3 Se7	2.485(2)	Se6 Hg2 Se5	113.35(7)	Hg4 Se4 Hg1	109.40(6)
Sn3 Se1	2.543(3)	Se6 Hg2 Se5	113.35(7)	Hg4 Se4 Hg1	109.40(6)
Hg4 Se4	2.5881(18)	Se6 Sn3 Se1	96.99(9)	Hg4 Se4 Hg2	110.35(7)
Hg4 Se7	2.630(2)	Se7 Sn3 Se6	115.70(6)	Hg4 Se4 Hg2	110.35(7)
Hg4 Se8	2.623(2)	Se7 Sn3 Se6	115.70(6)	Hg4 Se4 Hg4	107.78(10)
Hg4 Se9	2.641(2)	Se7 Sn3 Se7	115.23(11)	Sn1 Se5 Hg2	107.55(8)
Sn1 Se1	2.554(2)	Se7 Sn3 Se1	105.03(6)	Sn3 Se6 Hg2	102.48(9)
Sn1 Se2	2.514(3)	Se7 Sn3 Se1	105.03(6)	Sn3 Se7 Hg4	103.02(7)
Sn1 Se5	2.503(2)	Se4 Hg4 Se7	108.82(7)	Sn1 Se8 Hg4	103.37(7)
Sn1 Se8	2.491(2)	Se4 Hg4 Se8	109.79(7)	Sn2 Se9 Hg4	103.89(7)
Sn2 Se3	2.490(3)	Se4 Hg4 Se9	112.01(7)	Sn3 Se10 Sn	107.81(10)
Sn2 Se9	2.514(2)	Se7 Hg4 Se9	109.73(7)		
Sn2 Se9	2.514(2)	Se8 Hg4 Se7	107.18(7)		
Sn2 Se1	2.551(3)	Se8 Hg4 Se9	109.19(7)		
Se1 Sn1	2.554(2)	Se2 Sn1 Se1	107.59(6)		
Se3 Sn2	2.490(3)	Se5 Sn1 Se1	96.36(8)		
Se4 Hg4	2.5881(18)	Se5 Sn1 Se2	114.91(9)		
Se5 Sn1	2.503(2)	Se8 Sn1 Se1	107.57(8)		
Se8 Sn1	2.491(2)	Se8 Sn1 Se2	114.00(9)		
Se9 Sn2	2.514(2)	Se8 Sn1 Se5	114.37(10)		

Table S4. Comparison of photocurrent density performances for $(\text{H}_2\text{BPP})_2\text{CdSn}_3\text{Se}_9$ and $(\text{H}_2\text{DMP})_2\text{Hg}_4\text{Sn}_4\text{Se}_{15}$ with others reported chalcogenide systems

Sr#	Name of Compound	D	Photocurrent			Ref.
			I light ($\mu\text{A}/\text{cm}^2$)	Voltage	Sample	
1	$(\text{H}_2\text{BPP})_2\text{CdSn}_3\text{Se}_9$	1D	3.4 $\mu\text{A}/\text{cm}^2$ Visible Light	0.8	Film	This work
2	$(\text{H}_2\text{DMP})_2\text{Hg}_4\text{Sn}_4\text{Se}_{15}$	2D	2.39 $\mu\text{A}/\text{cm}^2$ Visible Light	0.8	Film	This work
3	$\text{Cs}_2\text{Ag}_2\text{Sb}_2\text{S}_5$	2D	4.5 $\mu\text{A}/\text{cm}^2$ Visible Light	-	Film	[S7]
4	$[\text{pipH}_2]_{0.5}[\text{Ag}_2\text{SbS}_3]$	2D	495 nA/cm ² Visible Light	0.6	powder	[S8]
5	$[\text{pipH}_2]_{0.5}[\text{Ag}_2\text{SbSe}_3]$	2D	430 nA/cm ² Visible Light	0.6	powder	[S8]
6	KCu_2SbS_3	2D	3.7 $\mu\text{A}/\text{cm}^2$ Visible Light	10	powder	[S9]
7	$[\text{Zn}(\text{tren})]_2\text{Sb}_2\text{Se}_5$	0D	1.10 $\mu\text{A}/\text{cm}^2$ Visible Light	-	Film	[S10]
8	$[\text{Zn}(\text{tepa})\text{H}]_2\text{Sb}_2\text{S}_6$	0D	0.95 $\mu\text{A}/\text{cm}^2$ Visible Light	-	Film	[S10]
9	$\text{Cs}_3\text{Sn}_3\text{Se}_{21}$	2D	1.2 $\mu\text{A}/\text{cm}^2$ Visible Light	0.8	Film	[S11]

pip = piperazine/ tren = tris (2-aminoethyl) amine/ tepa = tetraethylenepentamine

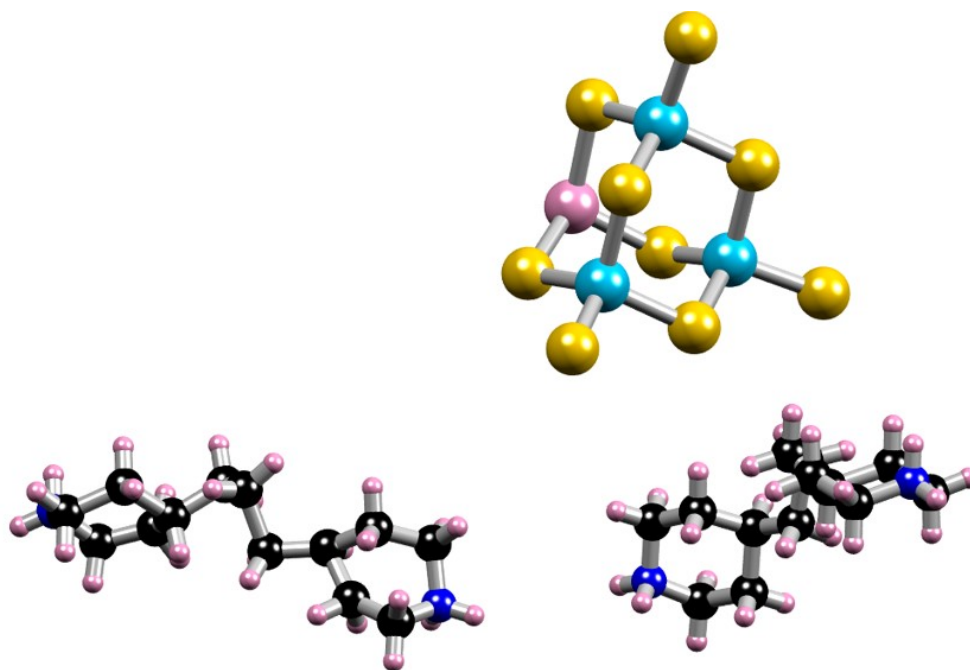


Figure S1. (a) Asymmetric unit of $(\text{H}_2\text{BPP})_2\text{CdSn}_3\text{Se}_9$ (hydrogen atoms are omitted for clarity)

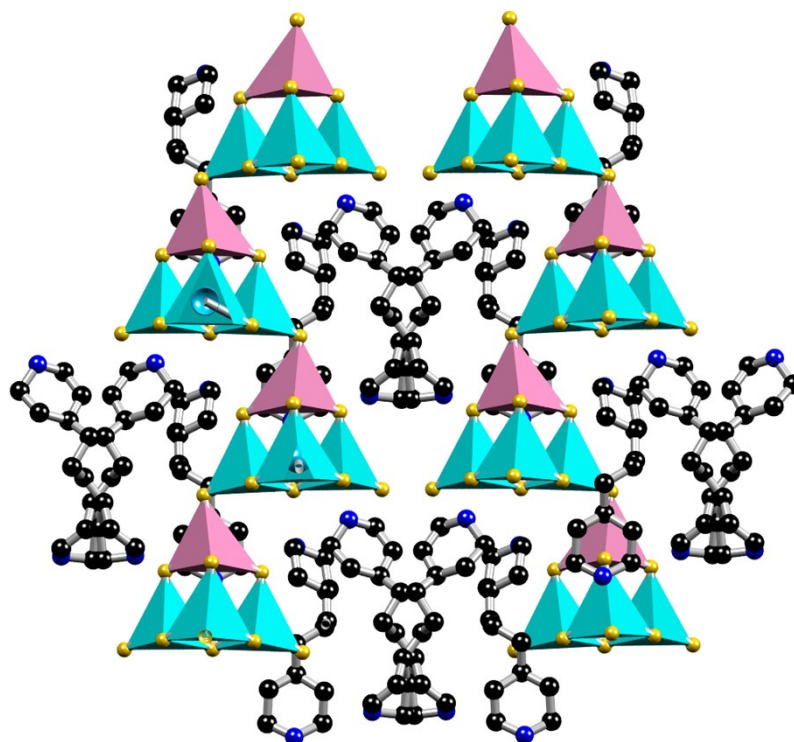


Figure S2. The crystal structure of 1D layered hybrid chalcogenides $(\text{H}_2\text{BPP})_2\text{CdSn}_3\text{Se}_9$ (hydrogen atoms are omitted for clarity).

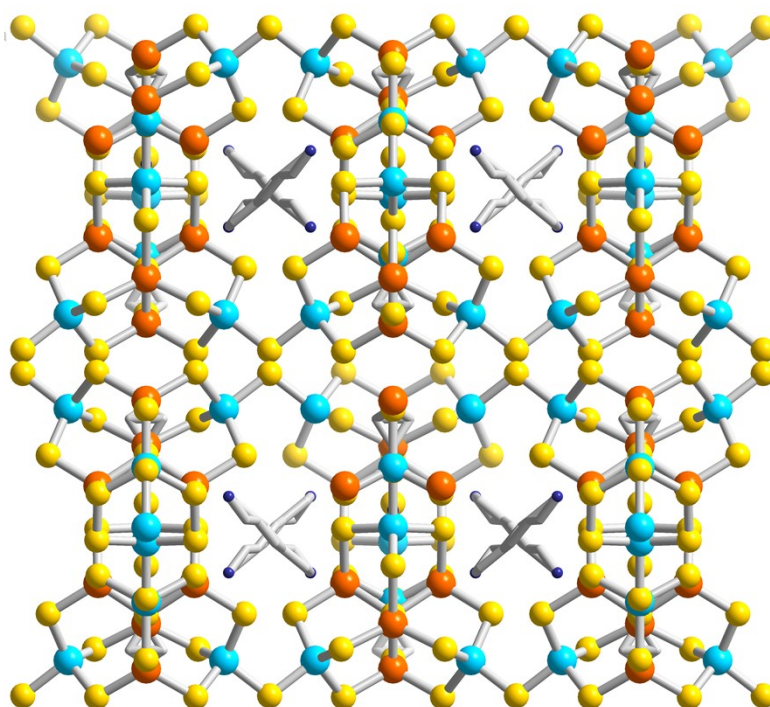


Figure S3. The crystal structure of 2D layered hybrid chalcogenides $(\text{H}_2\text{DMP})_2\text{Hg}_4\text{Sn}_4\text{Se}_{15}$ (hydrogen atoms are omitted for clarity).

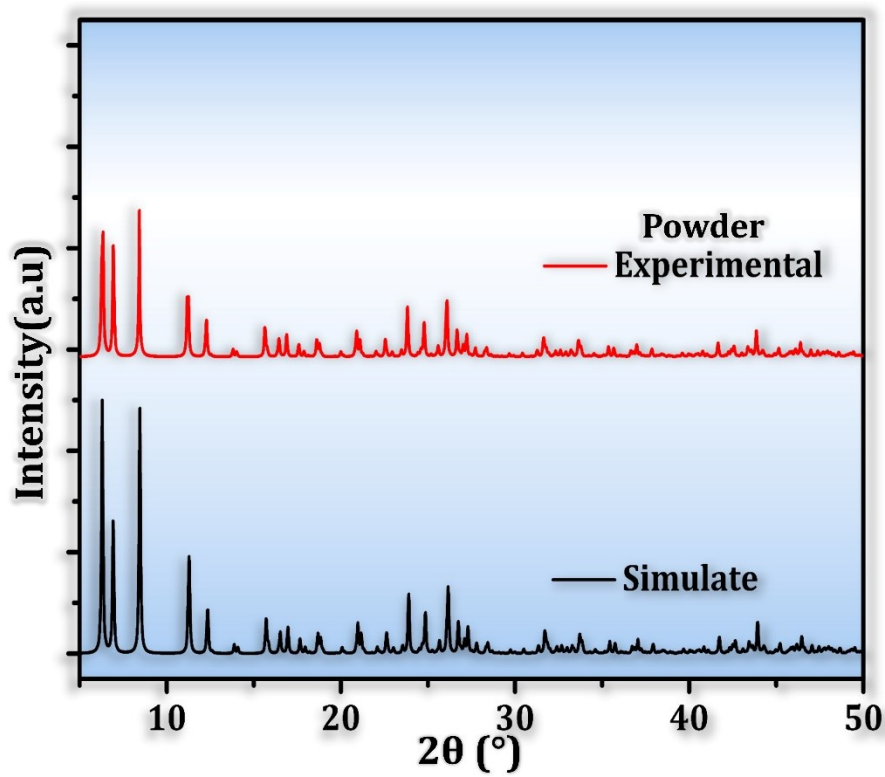


Figure S4. Powder XRD patterns of $(\text{H}_2\text{BPP})_2\text{CdSn}_3\text{Se}_9$.

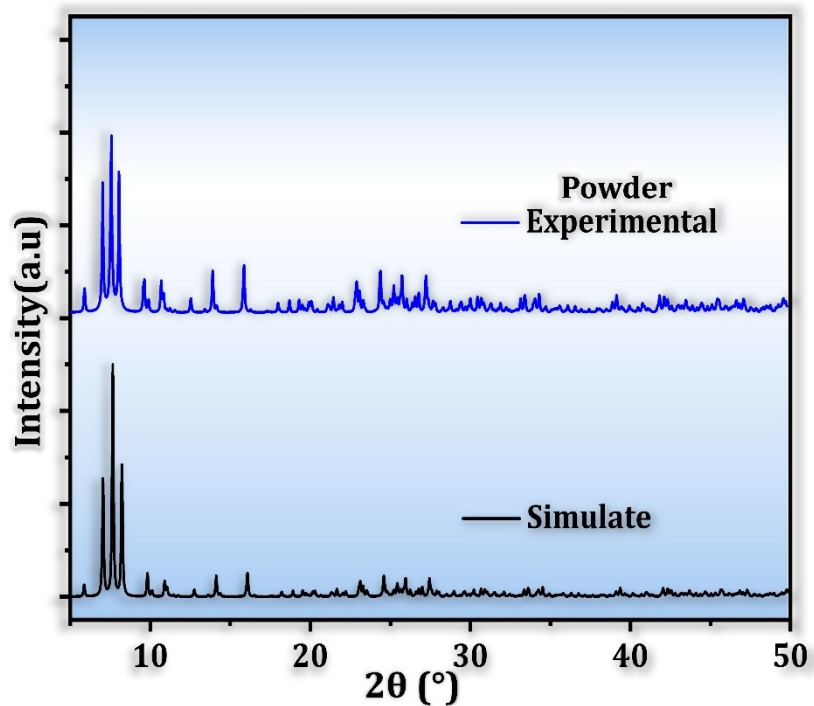


Figure S5. Powder XRD patterns of $(\text{H}_2\text{DMP})_2\text{Hg}_4\text{Sn}_4\text{Se}_{15}$

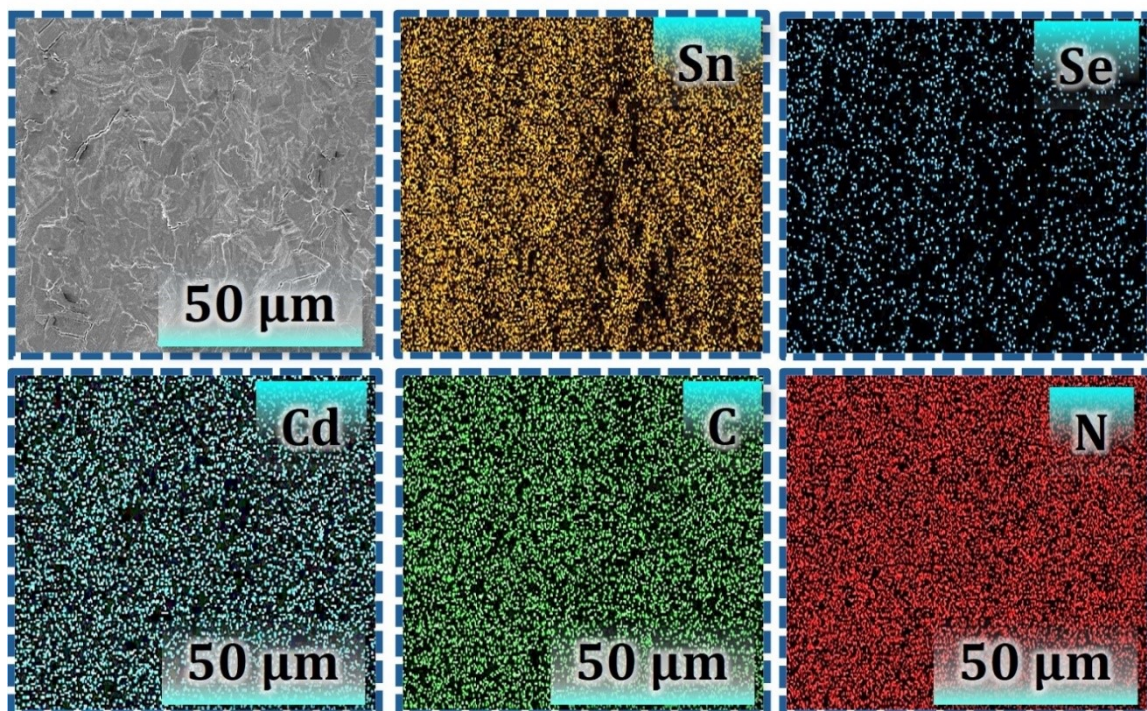


Figure S6. $(\text{H}_2\text{BPP})_2\text{CdSn}_3\text{Se}_9$ sample SEM and elemental mapping of Sb, Cl, C, N for a thin Film.

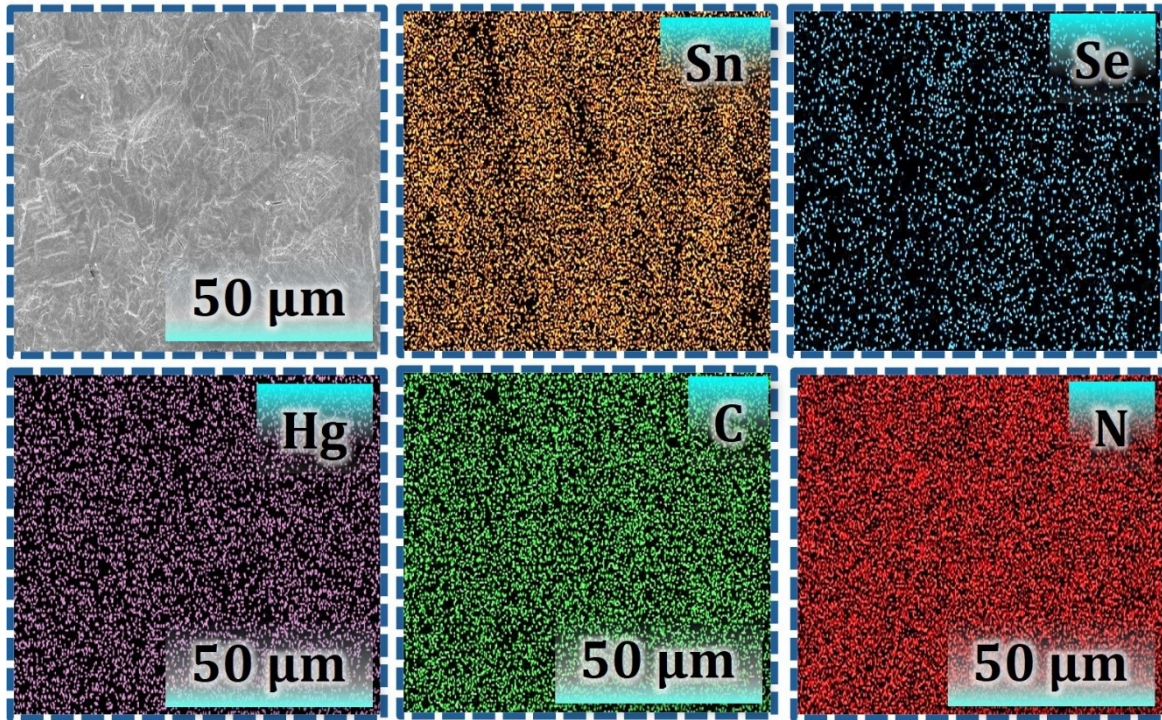


Figure S7. $(\text{H}_2\text{DMP})_2\text{Hg}_4\text{Sn}_4\text{Se}_{15}$ sample SEM and elemental mapping of Sb, Cl, C, N for a thin Film.

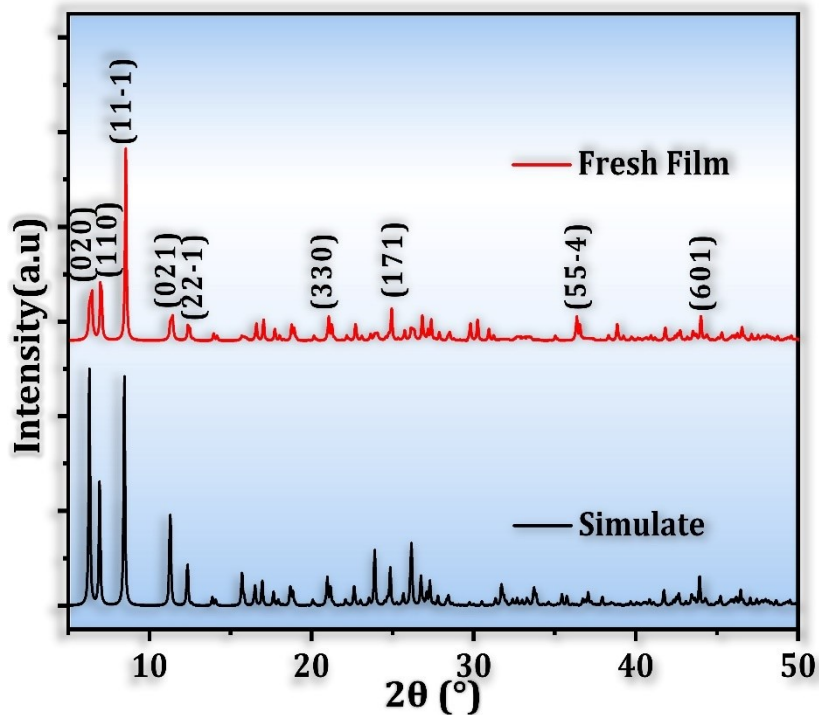


Figure S8. Thin Film XRD patterns of $(\text{H}_2\text{BPP})_2\text{CdSn}_3\text{Se}_9$

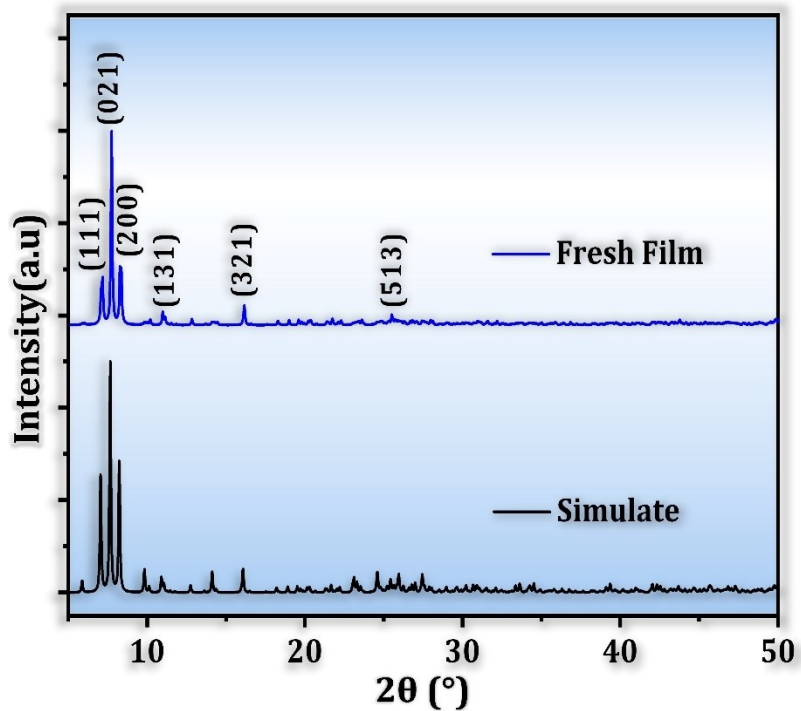


Figure S9. Thin Film XRD patterns of $(\text{H}_2\text{DMP})_2\text{Hg}_4\text{Sn}_4\text{Se}_{15}$

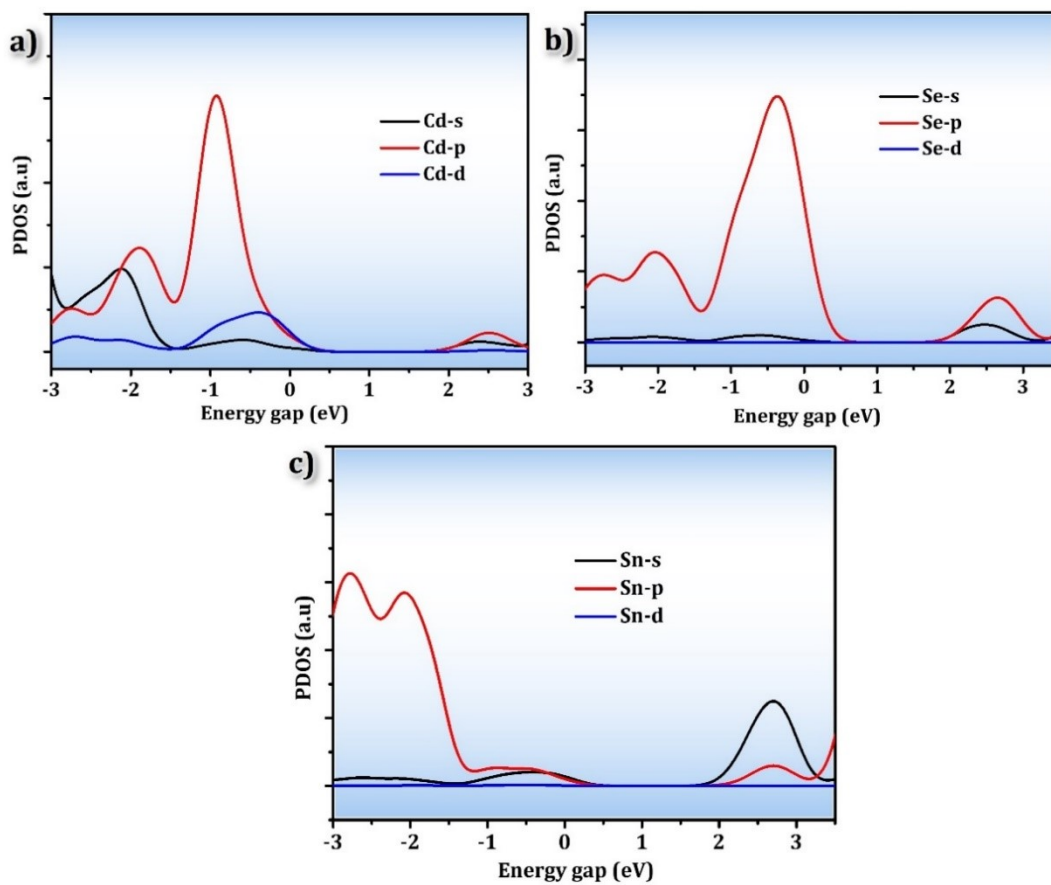


Figure S10. (a-c) Partial density of states (PDOS) of $(\text{H}_2\text{BPP})_2\text{CdSn}_3\text{Se}_9$ (Cd-s, Cd-p, Cd-d and Se-s, Se-p, Sn-s, Sn-p).

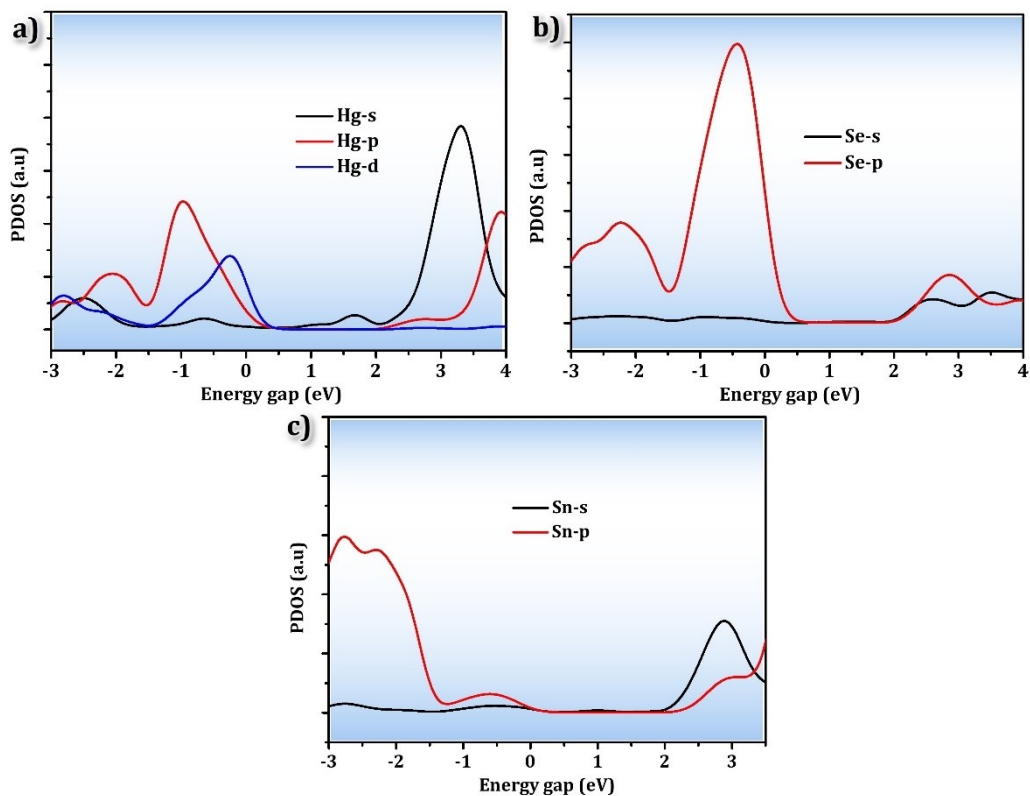


Figure S11. (a-c) Partial density of states (PDOS) of $(\text{H}_2\text{DMP})_2\text{Hg}_4\text{Sn}_4\text{Se}_{15}$ (Hg-s, Hg-p, Hg-d and Se-s, Se-p, Sn-s, Sn-p).

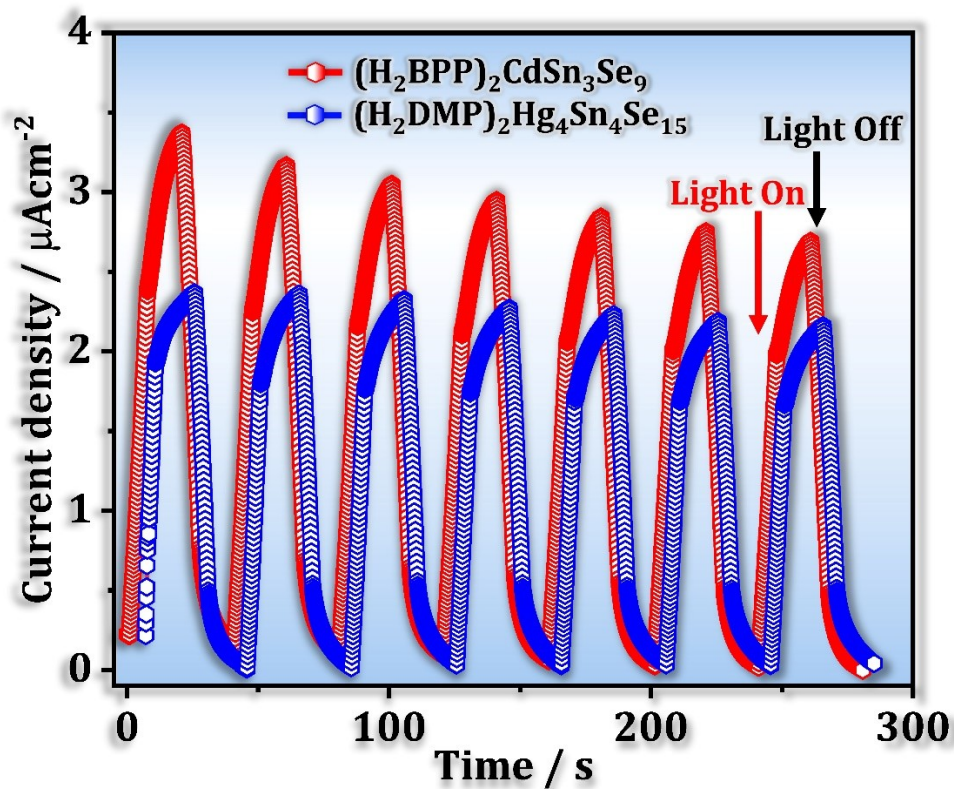
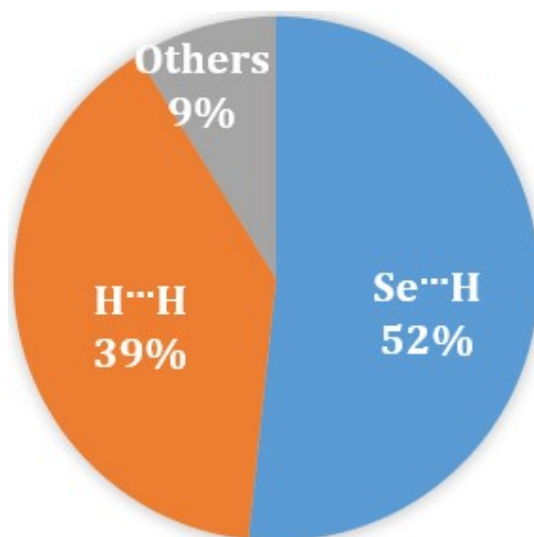


Figure S12. Photocurrent response under pulsed visible-light illumination at a constant potential of 0.8 V (vs. Ag/AgCl) for $(\text{H}_2\text{BPP})_2\text{CdSn}_3\text{Se}_9$ and $(\text{H}_2\text{DMP})_2\text{Hg}_4\text{Sn}_4\text{Se}_{15}$.



Intermolecular Interactions	$\text{H}\cdots\text{H}$	$\text{Se}\cdots\text{H}$	Others
Percentages	39.8%	52.1%	8.9%

Figure S13. The population of close contact of $(\text{H}_2\text{BPP})_2\text{CdSn}_3\text{Se}_9$ in crystal stacking.

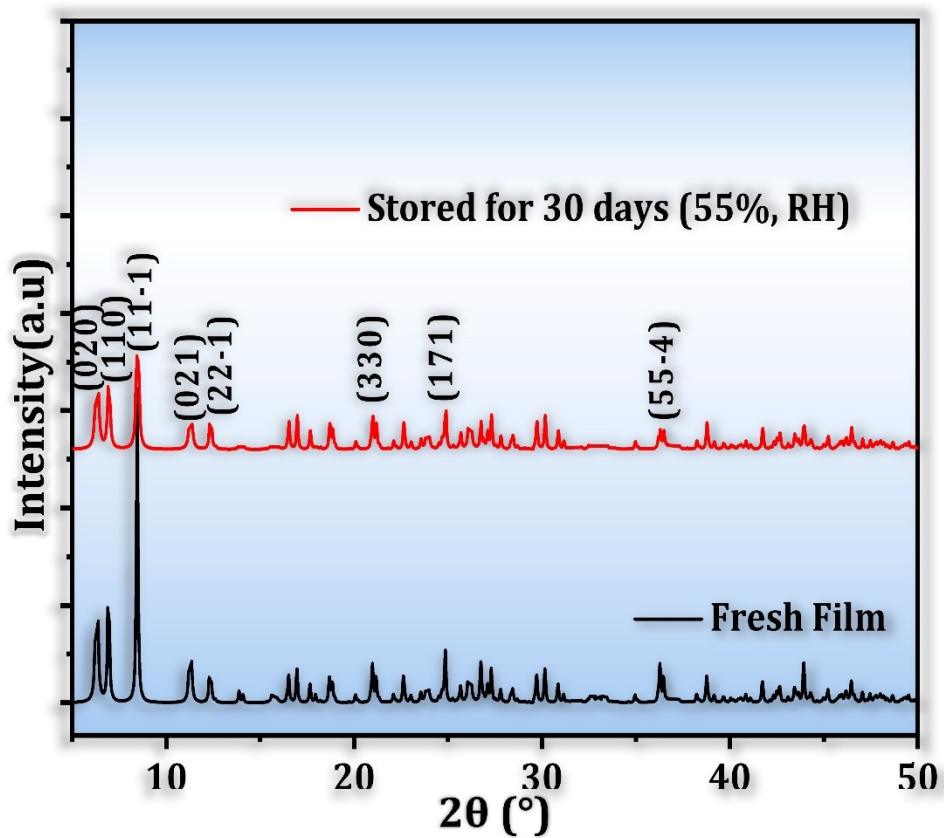


Figure S14. Stability of $(\text{H}_2\text{BPP})_2\text{CdSn}_3\text{Se}_9$ towards humidity showing PXRD of $(\text{H}_2\text{BPP})_2\text{CdSn}_3\text{Se}_9$ before and after exposure to 55% relative humidity

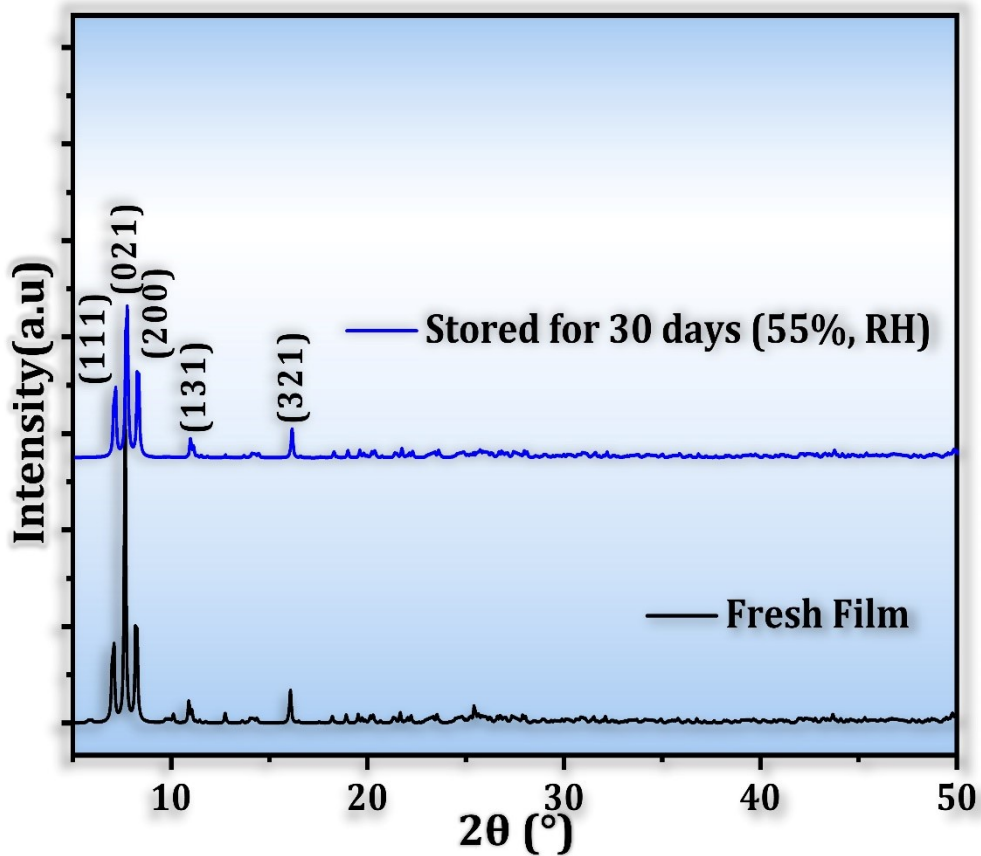


Figure S15. Stability of $(\text{H}_2\text{DMP})_2\text{Hg}_4\text{Sn}_4\text{Se}_{15}$ towards humidity showing PXRD of $(\text{H}_2\text{DMP})_2\text{Hg}_4\text{Sn}_4\text{Se}_{15}$ before and after exposure to 55% relative humidity

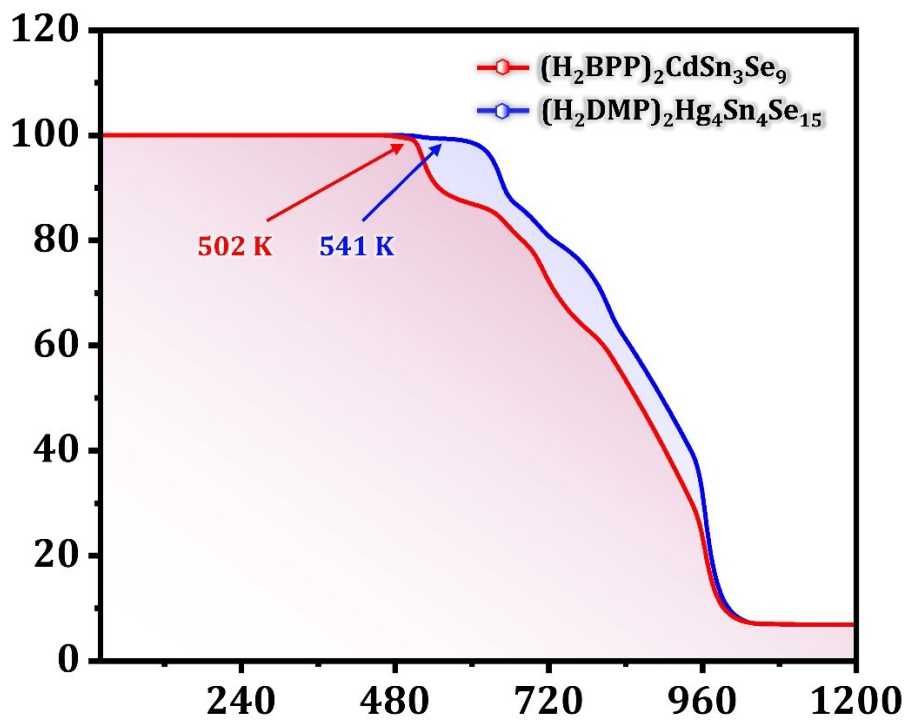


Figure S16. TGA curves of $(\text{H}_2\text{BPP})_2\text{CdSn}_3\text{Se}_9$ and $(\text{H}_2\text{DMP})_2\text{Hg}_4\text{Sn}_4\text{Se}_{15}$

4. References

- [S1] G. M. Sheldrick, *Acta Crystallogr A* **2008**, *64*, 112-122.
- [S2] F. E. M. O'BRIEN, The Control of Humidity by Saturated Salt Solutions, *J. Sci. Instrum.* **1948**, *25*, 73-76.
- [S3] J. Hafner, *J. Comput. Chem.* **2008**, *29*, 2044-2078.
- [S4] Perdew J P, Burke K, Ernzerhof M. Generalized Gradient Approximation Made Simple [J]. *Physical Review Letter.* **1996**, *77*(18), 3865-3868.
- [S5] D. M. Ceperley and B. J. Alder, Ground-state of the electron-gas by a stochastic method. *Phys. Rev. Lett.* **1980**, *45*, 566.
- [S6] J. P. Perdew and A. Zunger, *Phys. Rev. B: Condens. Matter Mater. Phys.* **1981**, *23*, 5048.
- [S7] Y. Liu, C. Yu, Z. Xie, M. Cao, D. Miao, Z. Xue and Y. Li, *Dalton Transactions*, 2024, **53**, 16149-16153.
- [S8] H. Wang, J.-M. Yu, N. Wang, L.-L. Xiao, J.-P. Yu, Q. Xu, B. Zheng, F.-F. Cheng and W.-W. Xiong, *Journal of Solid State Chemistry*, 2021, **300**, 122276.
- [S9] R. Wang, X. Zhang, J. He, C. Zheng, J. Lin and F. Huang, *Dalton Transactions*, **2016**, **45**, 3473-3479.
- [S10] L. Zhang, H. Zhao, X. Liu, G. Teri and M. Baiyin, *Physical Chemistry Chemical Physics*, **2023**, *25*, 29709-29717.
- [S11] T. Wang, H. Zhao, Y.-Q. Hu, S. Ding, Z. Zhang, G.-Y. Gou, M. S. Lassoued and Y.-Z. Zheng, *ACS Applied Energy Materials*, **2024**, *7*, 2847-2853.